Electrospun NaMnPO4–carbon nanofiber composite: a novel freestanding cathode for Na-ion batteries

Journal of Energy Storage 174 (2026) 123131

Contents lists available at ScienceDirect

Journal of Energy Storage

journal homepage: www.elsevier.com/locate/est

Research papers

# Electrospun $NaMnPO_4$–carbon nanofiber composite: a novel freestanding cathode for Na-ion batteries☆

Leone Frusteri [a], Emanuele La Mazza [a], Mayank Joshi [a,b], Orazio Di Blasi [a], Alessandra Di Blasi [a], Concetta Busacca [a,*]

[a] CNR-Istituto di Tecnologie Avanzate per l'Energia "Nicola Giordano" (ITAE), Salita S. Lucia sopra Contesse, 5-98126, Messina, Italy
[b] Department of Applied Science and Technology (DISAT), Politecnico di Torino, Corso Duca degli Abruzzi 24, 10129, Turin, Italy

ARTICLE INFO

*Keywords:*
Sodium-ion batteries
Freestanding cathode
Electrospinning
Flexible cathode
Carbon nanofibers
$NaMnPO_4$ composite
Dual-phase
Maricite–olivine

ABSTRACT

Flexible, binder-free electrodes are increasingly attractive for next-generation sodium-ion batteries, where lightweight architectures and simplified processing can increase energy density and reduce costs. Here, we present a freestanding $NaMnPO_4$–carbon nanofiber ($NaMnPO_4$–CNF) cathode obtained through a single-step electrospinning process that simultaneously forms the active phase and the electrode, eliminating binders, conductive additives and metallic current collectors. Structural analyses reveal a mixed maricite–olivine $NaMnPO_4$ phase uniformly embedded within a conductive N-doped CNF network. The resulting fibrous architecture exhibits hierarchical porosity and a high surface area (119 $m^2\ g^{-1}$), which promote electrolyte infiltration and fast $Na^+$ transport. When tested in Na-ion half-cells, the $NaMnPO_4$–CNF electrode delivers ~143 mAh $g^{-1}$ at 0.1C (92% of the theoretical capacity) and retains ~135, ~110 and ~ 90 mAh $g^{-1}$ at 0.5C, 1C and 2C, respectively, with Coulombic efficiencies above 95%. Long-term cycling confirms excellent durability, with ~140 mAh $g^{-1}$ at 0.1C, ~125 mAh $g^{-1}$ at 0.5C and ~ 80 mAh $g^{-1}$ at 2C after 500 cycles. Post-mortem analyses show that, despite progressive amorphization of the $NaMnPO_4$ phase, the CNF matrix preserves structural integrity and elemental homogeneity. Compared with previously reported maricite $NaMnPO_4$ cathodes, the freestanding $NaMnPO_4$–CNF electrode offers markedly improved capacity, rate performance and cycling stability across a broader current range. This work demonstrates, for the first time, a dual-phase $NaMnPO_4$ cathode integrated into an electrospun, binder-free architecture with state-of-the-art performance, opening a promising route toward flexible, energy-dense and low-cost sodium-ion batteries.

## 1. Introduction

The urgent need to mitigate climate change and phase out fossil fuels is driving the rapid deployment of renewable energy sources to meet decarbonization targets set for 2050 [1,2]. Their intermittency requires efficient energy storage systems (ESS) to ensure stable grid integration [3–6]. While lithium-ion batteries (LIBs) dominate the market, concerns over cost, sustainability, and safety have motivated alternative technologies. Sodium-ion batteries (NIBs) are attractive due to sodium abundance, lower cost, and "drop-in" compatibility with current LIB manufacturing [7–10]. However, the larger ionic radius and higher mass of $Na^+$ (1.02 Å, 23 g $mol^{-1}$) result in slower kinetics, lower voltage (~2.5 vs. 3.7 V) and reduced energy density (~150 vs. 250 Wh $kg^{-1}$), highlighting the need for cathode materials with enhanced structural stability, conductivity and active sites [11–13]. An effective strategy involves coupling one-dimensional (1D) nanostructured materials with conductive carbonaceous or polymeric matrices, which provide continuous electron pathways, short $Na^+$ diffusion lengths, and mechanical strength [14–17]. Electrospinning is an attractive synthesis method because it enables controlled 1D morphologies with interconnected 3D conductive networks, and direct incorporation of carbon or polymer components during synthesis [18–20]. Recent studies have shown excellent stability and rate capability in electrospun cathodes based on $Na_{0.44}MnO_2$ and $NaCrO_2$ [21,22], as well as in flexible and binder-free systems based on $Na_4Fe_2(PO_4)_2(P_2O_7)$/C and $NaFePO_4$@C composites [23,24]. These developments align with increasing industrial interest in flexible energy storage, with major companies such as Samsung, LG, and 3 M investing in the field [25]. In the specific case of

☆ This article is part of a Special issue entitled: 'ICSET 2025-Energy Storage' published in Journal of Energy Storage.

* Corresponding author.
*E-mail address:* concetta.busacca@itae.cnr.it (C. Busacca).

https://doi.org/10.1016/j.est.2026.123131
Received 27 November 2025; Received in revised form 18 May 2026; Accepted 10 June 2026
Available online 17 June 2026

NIBs, flexible architectures eliminate metal current collectors and binders, which increases energy density and simplifies manufacturing [26,27]. Guided by this technological trend, we developed a flexible, freestanding $NaMnPO_4$–carbon nanofiber ($NaMnPO_4$–CNF) cathode synthesized by electrospinning. Compared to the widely studied $NaFePO_4$, $NaMnPO_4$ provides higher $Mn^{2+}/Mn^{3+}$ redox potential (~3.8 V vs. $Na^+/Na$) and greater theoretical capacity (155 mAh $g^{-1}$) while remaining cost-effective and environmentally friendly. Moreover, manganese is an attractive element due to its abundance, low toxicity, and relatively lower criticality compared to other transition metals such as Co, although it has recently been included in the EU list of critical raw materials. It is still considered strategically important for battery supply chains. Its high theoretical capacity further enhances its appeal for sodium-ion storage. However, its practical application has been limited by phase stability issues, as the thermodynamically stable maricite structure is electrochemically inactive, whereas the active olivine phase is difficult to obtain in pure form. Previous studies have attempted to overcome the intrinsic inactivity of the maricite phase by activation with the olivine phase. Mohsin et al. [28] obtained partial olivine formation from commercial maricite $NaMnPO_4$ after ball milling and carbon coating, but the material delivered only a specific capacity ~47 mAh $g^{-1}$ at 0.1C. Priyanka et al. explored both solid-state and polyol synthesis to activate $NaMnPO_4$ maricite. Solid-state synthesis produced nanosized $NaMnPO_4$ with agglomerates, delivering a specific capacity of ~30 mAh $g^{-1}$ at 0.1C, decreasing to ~18 mAh $g^{-1}$ after 50 cycles [29]. Polyol synthesis, through control of the diol chain length [30] or acetate precursors [31], produced highly crystalline rod-shaped particles, reaching a specific capacity of ~102 mAh $g^{-1}$ at 0.1C, decaying to ~70 mAh $g^{-1}$ after 50 cycles. In all cases, performance remained limited by particle agglomeration and sluggish $Na^+$ transport. Our work addresses these limitations through an appropriate synthesis method that allows control of the phase composition and electrode architecture. In particular, the novelty of this work lies in the simultaneous integration of phase engineering and electrode architecture design, achieved through the synergistic combination of a controlled mixed olivine–maricite $NaMnPO_4$ phase with a conductive N-doped CNF network, enabling enhanced electrochemical kinetics, structural stability, and high-rate performance in a flexible, binder-free configuration. In addition, the proposed strategy combines simplified processing, structural design, and mechanistic understanding of charge storage, providing a comprehensive approach for the development of high-performance $NaMnPO_4$-based cathodes. We successfully stabilized a mixed olivine-maricite phase $NaMnPO_4$ uniformly embedded in a conductive carbon nanofiber (CNF) network. Crucially, electrospinning enabled simultaneous synthesis of the active material and fabrication of a flexible, freestanding electrode, eliminating ink preparation, binders, carbon additives, Al-foil coating, and drying. This streamlined route lowers processing complexity and cost while boosting gravimetric energy density. The obtained electrochemical performance significantly improves on previously reported $NaMnPO_4$-based systems. The developed $NaMnPO_4$–CNF electrode delivers high specific capacity (~143 mAh $g^{-1}$ at 0.1C) and excellent cycling stability, demonstrating competitive performance compared to previously reported $NaMnPO_4$-based systems. To the best of our knowledge, this is the first demonstration of a binder-free electrospun $NaMnPO_4$ cathode with a stable mixed maricite–olivine structure delivering state-of-the-art performance. By integrating phase control with a conductive N-doped carbon nanofiber network, the proposed approach enables improved electrochemical kinetics and structural stability in a flexible, freestanding configuration. This strategy combines simplified processing, optimized electrode architecture, and enhanced charge storage mechanisms, providing new insights into the design of high-performance $NaMnPO_4$-based cathodes for sodium-ion batteries.

## 2. Experimental

### 2.1. Starting materials

All reagents were purchased from Sigma-Aldrich and used without any further purification. Polyacrylonitrile (PAN, $M_W$ 150,000) served as the carbon nanofibers (CNFs) precursor. Sodium acetate ($CH_3COONa$), manganese (II) acetate tetrahydrate ($(CH_3COO)_2Mn{\cdot}4H_2O$) and phosphoric acid ($H_3PO_4$, 85 wt% in $H_2O$) were used as sodium, manganese and phosphate sources to synthesize $NaMnPO_4$. *N*,*N*-dimethylformamide (DMF) was used as the solvent for polymer dispersion.

### 2.2. Material preparation

Two precursor solutions were first prepared. Solution A contained 1.2 g of PAN dissolved in 11 g of DMF. Solution B comprised equimolar sodium acetate, manganese(II) acetate, and phosphoric acid dispersed in 9 g of DMF. Both solutions were magnetically stirred at room temperature for 2 h to ensure complete dissolution. Subsequently, the $NaMnPO_4$ precursor solution (B) was added dropwise to solution Aunder continuous stirring until a homogeneous and clear mixture was obtained. This solution was loaded into a 20 mL glass syringe equipped with a stainless-steel needle, placed at a distance of 12 cm from the collector, and electrospun at 1 mL $h^{-1}$ (peristaltic pump) under a 17 kV electric field, producing a polymeric membrane. The latter was subjected to two successive thermal treatments consisting of stabilization at 270 °C in air for 30 min and carbonization at 600 °C for 1 h under a reducing $H_2/N_2$ atmosphere (5:95).

### 2.3. Material characterization

Differential scanning calorimetry (DSC) and thermogravimetric (TG) analyses were performed in static air using a 409C NETZSCH-Gerätebau GmbH analyser to quantify the $NaMnPO_4$ content in the sample after total CNF combustion. Measurements were performed from 20 to 1200 °C at 10 °C $min^{-1}$. Phase and structural characterization was performed by X-ray diffraction (XRD) using a Bruker D8 Advance system with monochromatic Cu Kα radiation ($\lambda = 1.5406$ Å, 40 kV, 40 mA), and phase identification was achieved by comparison with literature data. Rietveld refinement of the XRD data was performed using Cu Kα radiation. The diffraction patterns were fitted using orthorhombic Pnma structural models for both maricite- and olivine-type $NaMnPO_4$. The peak profiles were described using a pseudo-Voigt function with Caglioti (U, V, W) parameters to account for instrumental and sample broadening. The background was modelled using a six-term Chebyshev polynomial. Scale factors, lattice parameters, and profile parameters were refined to achieve the best fit between observed and calculated patterns. Surface chemical composition was investigated by X-ray photoelectron spectroscopy (XPS) using a Physical Electronics 5800–01 spectrometer equipped with a monochromatic Al Kα source. XPS spectra were collected at a pass energy of 58.7 eV under a chamber pressure of $10^{-9}$ Torr, and peak fitting was performed with PHI Multipak 6.1. Morphology was examined by scanning electron microscopy (SEM) with a Philips XL30 S FEG microscope on samples cast onto aluminum stubs, followed by qualitative/quantitative analysis and elemental mapping via EDX at 20 kV. Additional transmission electron microscopy (TEM) and EDX analyses were carried out on a JEOL F200 microscope at 200 kV using samples drop-cast onto holey carbon-coated Cu grids from an isopropanol suspension. The structural features of the samples were further investigated by Raman spectroscopy using a DXR3 confocal Raman microscope (Thermo Fisher Scientific). Spectra were collected at room temperature using a 532 nm excitation laser with a 20× objective and an incident power of 2 mW. Specific surface area was determined using the BET method from $N_2$ adsorption–desorption isotherms at −196 °C (ASAP 2020 M Micromeritics), and pore size distribution was obtained by the BJH model.

### 2.4. Electrochemical measurements

Electrochemical performance was evaluated by cyclic voltammetry (CV) and galvanostatic charge-discharge (GCD) tests. CV measurements were conducted on a BiologicVSP-3e Potentiostat at 0.1 mV $s^{-1}$ in the voltage range of 1.0–3.5 V vs. $Na/Na^+$ at room temperature. GCD tests were carried out on a BST8-MA channel battery analyser (MTI Corp.) within a potential window of 1.5–3.5 V versus $Na^+/Na$ at various current rates. Current densities and specific capacities of the $NaMnPO_4$–CNF electrode were calculated based on the mass of $NaMnPO_4$ active material, excluding the CNF mass contribution. Pristine CNFs were also tested under the same cell configuration and voltage window, from 1.5 to 3.5 V vs. $Na^+/Na$, to evaluate their electrochemical contribution. The materials were cut into 2 $cm^2$ discs and directly assembled as cathodes in the cells, with a mass loading of approximately 5 mg $cm^{-2}$, without the use of carbon additives, binders, or Al foil. CR2032 coin cells were employed for this study, assembled in a nitrogen-filled glove box with a thin layer of metallic sodium as the counter/reference electrode in a half-cell configuration. The electrolyte consisted of a 1 M $NaPF_6$ solution in a 1:1 mixture of ethylene carbonate and diethyl carbonate, and a glass fiber membrane (Whatman, GF/A) was used as the separator. Electrochemical measurements were performed on three independently assembled coin cells prepared using the same batch of active material to ensure reproducibility.

## 3. Results and discussion

### 3.1. Physico-chemical characterization results

The electrospinning process enabled the direct fabrication of a $NaMnPO_4$–CNF membrane without the typical slurry-based steps such as mixing, coating, drying, and solvent recovery. After carbonization, the membrane was cut into freestanding cathode and directly assembled into Na-ion coin cell, highlighting the simplicity and scalability of the method (Fig. 1a). The XRD pattern of the electrospun $NaMnPO_4$–CNF composite is shown in Fig. 1b. The diffraction peaks confirm the coexistence of maricite-type (m-$NaMnPO_4$) and olivine-type (o-$NaMnPO_4$) polymorphs, in agreement with literature reports [32]. Rietveld refinement shows good agreement between the observed and calculated profiles, as indicated by the low residual values (Rwp = 3.89%, Rp = 2.21%, Rexp = 10.26%, $\chi^2 = 0.379$). The refined structural parameters and phase fractions are summarized in Table 1. The lattice parameters are consistent with previously reported values for both polymorphs. The phase composition corresponds to 21.3 wt% maricite and 78.7 wt% olivine, confirming the predominance of the electrochemically active olivine phase in the bulk material. Minor discrepancies in the relative intensities of some reflections can be attributed to peak overlap between the two polymorphs, preferred orientation effects, and the nanostructured nature of the electrospun composite. A broad feature centred at approximately $2\theta \approx 25°$ is assigned to the amorphous carbon originating from the CNF network.

Thermal analysis further supports the formation of the composite (Fig. 1c). A small weight loss near 100 °C corresponds to removal of adsorbed water and residual solvent. The main weight loss, characterized by a double exothermic peak, occurs between 400 °C and 600 °C and is linked to the complete combustion of carbon nanofibers. This weight loss is proportional to the amount of $NaMnPO_4$ in the sample. No additional weight losses are observed above 600 °C in the TGA profile. In contrast, the DSC profile reveals two endothermic peaks at approximately 730 °C and 830 °C. The first peak corresponds to the decomposition or transformation of m-$NaMnPO_4$ into new phases due to impurities, while the second peak is associated with the melting of m-

**Table 1**
Refined structural parameters and phase fractions obtained from Rietveld analysis of the $NaMnPO_4$–CNF composite.

| Phase | a(Å) | b (Å) | c (Å) | V ($Å^3$) | wt% |
|---|---|---|---|---|---|
| Maricite $NaMnPO_4$ | 9.067 | 6.898 | 5.085 | 318.0 | 21.3 |
| Olivine $NaMnPO_4$ | 10.574 | 6.208 | 4.909 | 322.2 | 78.7 |

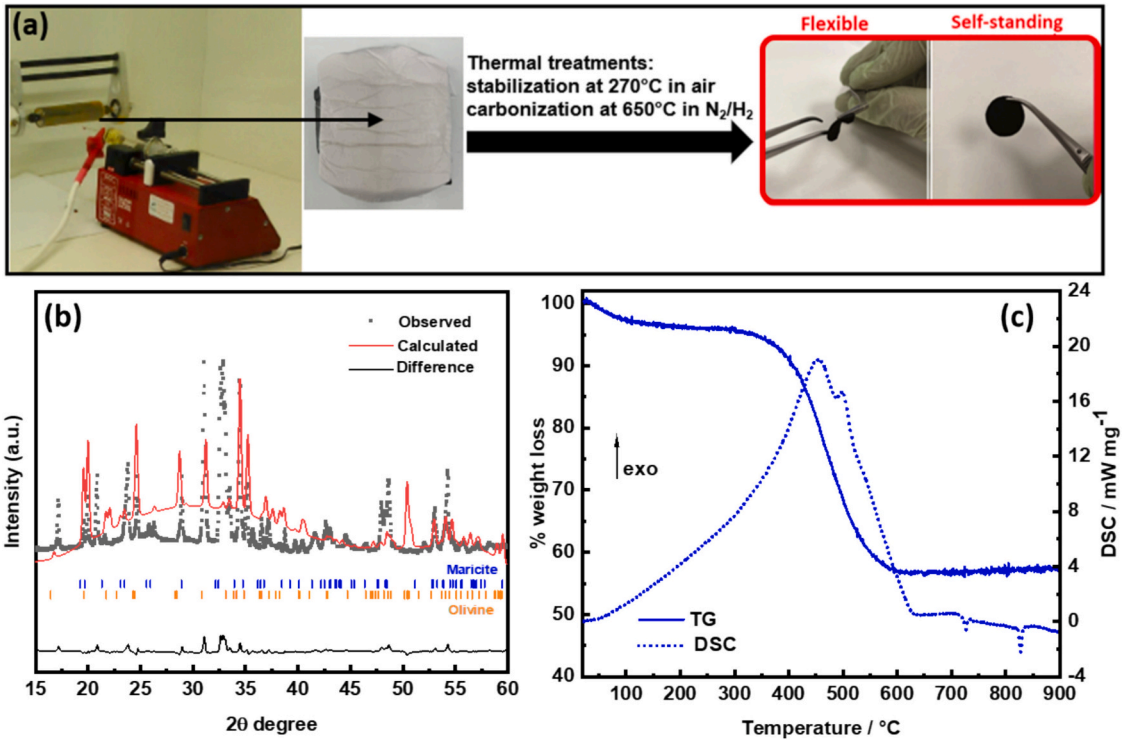


**Fig. 1.** (a) Schematic illustration of the electrospun $NaMnPO_4$-CNF electrode and its preparation process; (b) XRD pattern with Rietveld refinement and (c) TGA/DSC analysis of the sample.

$NaMnPO_4$ [28].

SEM analysis reveals a dense and interconnected fibrous structure, as evident from the low-magnification micrograph in Fig. 2a. The corresponding fiber diameter distribution (Fig. 2b), fitted with a Gaussian function, gives an average value of ~352 nm. Higher-magnification analysis (Fig. 2c) reveals the formation of small clusters, a few tens of nanometres in size, distributed along the fiber surfaces. Edge-view imaging of an individual nanofiber (Fig. 2d) further confirms that these clusters extended throughout the cross-section rather than being confined to the outer surface, suggesting a uniform distribution of $NaMnPO_4$ within the CNF matrix. Further magnified images (Fig. 2e,f) reveal a high density of nanopores distributed across the fiber surface,

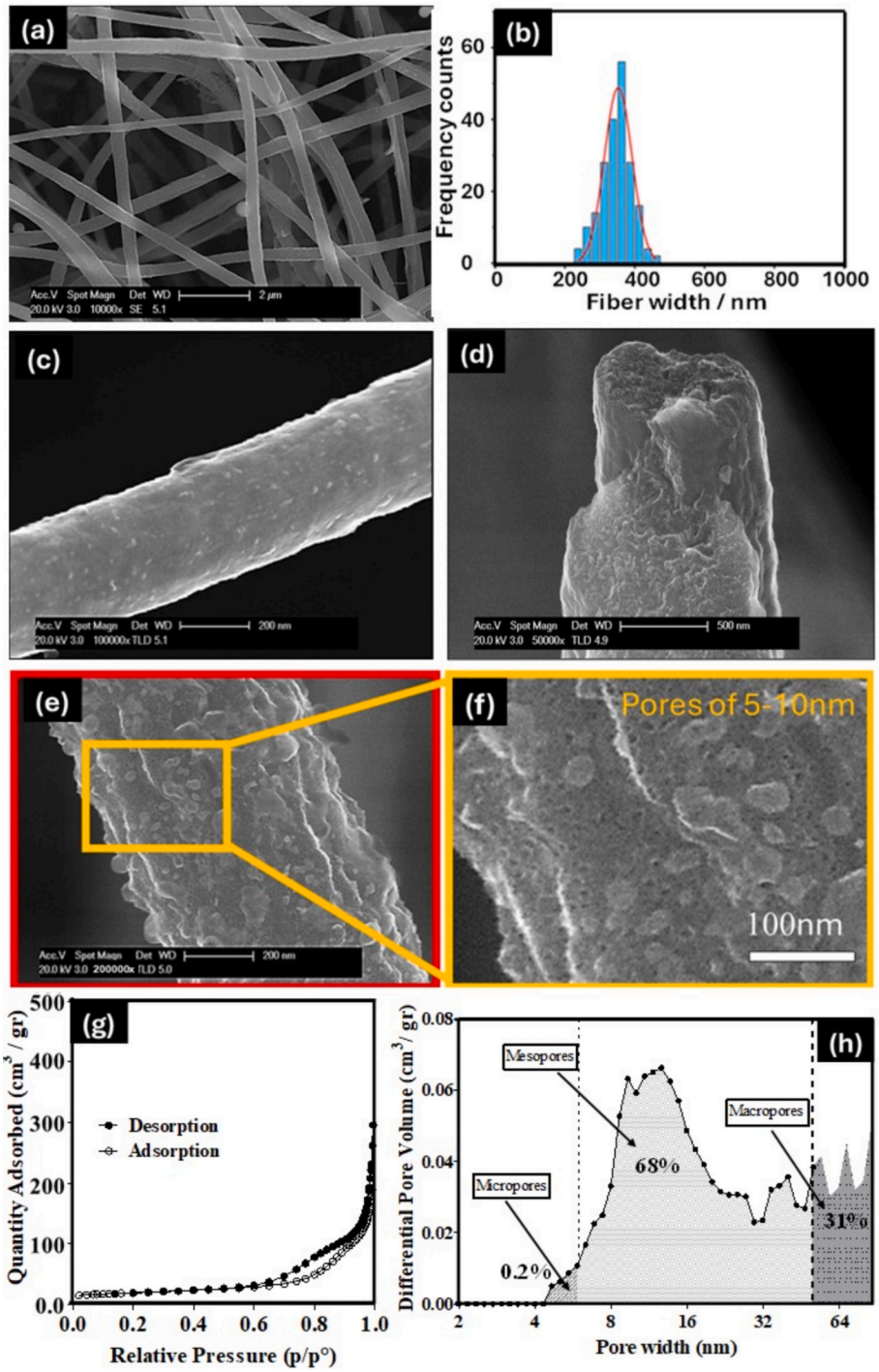


**Fig. 2.** (a) Low-magnification SEM image; (b) fiber diameter distribution histogram; (c) high-magnification SEM image of a single fiber; (d) SEM micrograph of a fiber edge; (e) very high magnification SEM image highlighting the surface morphology; (f) enlarged view showing nanoscale pores; (g) $N_2$ adsorption–desorption isotherms; (h) corresponding pore size distribution. EDX mapping analysis of the $NaMnPO_4$-CNF sample (Fig. 3a,b) shows a uniform distribution of Na, Mn, P, O and C across the entire nanofiber network. The elemental signals overlap throughout the fibers without localized enrichment, indicating that $NaMnPO_4$ is homogeneously embedded within the carbon matrix. Importantly, the nanoscale clusters observed in the SEM images do not correspond to any segregation of $NaMnPO_4$, confirming that the active phase is not deposited as surface agglomerates but is uniformly dispersed along the fibers. These findings are further supported by TEM/EDX analysis (Fig. 3c), which confirmed a homogeneous distribution of carbon and $NaMnPO_4$ within individual nanofibers.

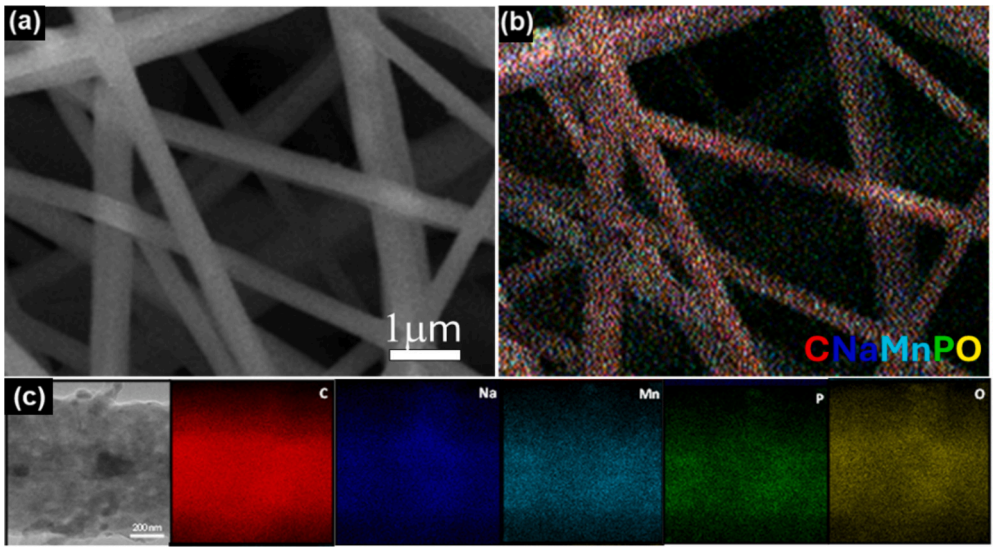


**Fig. 3.** (a-b) EDX mapping TEM image; (c) EDX mapping analysis of $NaMnPO_4$-CNF sample.

with diameters in the 5–10 nm range, confirming the porous nature of the composite. Such morphology as well as porosity is expected to shorten ion-diffusion pathways and facilitate electrolyte penetration within the electrode. The porous structure is further supported by nitrogen adsorption–desorption measurements (Fig. 2g), where the $N_2$ isotherm exhibits a typical type-IV profile with a pronounced hysteresis loop in the 0.4–1.0 $P/P^0$ region, characteristic of mesoporous materials. The corresponding BET surface area was 119 $m^2\ g^{-1}$. The pore size distribution (Fig. 2h) confirms the presence of a hierarchical pore system, including micro- and mesopores.

XPS analysis enables the identification of the surface chemical composition and oxidation states of the electrospun composite. The survey spectrum (Fig. 4a) and the corresponding quantitative analysis (inset) show the expected signals of Na 1 s, Mn 2p, P 2p, O 1 s, C 1 s and N 1 s at their characteristic binding energies, confirming the successful formation of the $NaMnPO_4$ phase embedded within the CNF matrix. The elemental ratios are consistent with the expected stoichiometry of the composite at the surface level. The Mn 2p core-level spectrum (Fig. 4b), exhibits two broad peaks in the ranges of 640.8–642.8 eV and 652.6–654.4 eV, corresponding to Mn $2p_{3/2}$ and Mn $2p_{1/2}$, respectively. Fitting of the Mn $2p_{3/2}$ region revealed two peaks at binding energies of 641.8 eV and 642.05 eV, which are attributed to $Mn^{2+}$ in maricite-$NaMnPO_4$ and olivine-$NaMnPO_4$ structures, respectively [30]. These findings confirm the coexistence of the two polymorphs identified by XRD analysis. The presence of a satellite peak between 645.0 eV and 647.0 eV further supports the stabilization of manganese in the +2 oxidation state [31]. The C 1 s spectrum (Fig. 4c) displays four contributions at 284.6, 285.2, 286.6 and 288.6 eV, assigned to C═C, C—C, C═O/C═N and C—O bonds, respectively. The presence of C═C and C—C confirms a mixed graphitic/amorphous carbon structure, while the C═N contribution indicates that nitrogen was successfully incorporated into the carbon matrix. The N 1 s spectrum (Fig. 4d) further corroborates the existence of various nitrogen species, including N-pyridinic, N-pyrrolic, and N-graphitic, as evidenced by the three peaks centred at 398.5 eV, 400.7 eV, and 401.25 eV, respectively. Pyridinic and pyrrolic N-sites are generally regarded as defects that enhance $Na^+$ adsorption and diffusion, while graphitic nitrogen improves electronic conductivity. Therefore, the coexistence of these N-configurations is expected to facilitate both ion transport and charge transfer within the freestanding cathode. Raman spectroscopy was further performed to evaluate the degree of graphitization of the carbon nanofiber matrix (Fig. 4e). The spectrum exhibits two characteristic bands located at ~1350 $cm^{-1}$ (D band) and ~ 1580 $cm^{-1}$ (G band), corresponding to disordered carbon and graphitic domains, respectively. The intensity ratio ($I_D/I_G \approx 0.93$), obtained after baseline correction, indicates a partially graphitized carbon structure, typical of PAN-derived CNFs. This result is consistent with the XPS analysis of the C 1 s region, which confirms the coexistence of graphitic and amorphous carbon phases. Such a partially graphitized carbon network provides sufficient electronic conductivity to support the electrochemical performance of the electrode.

### 3.2. Electrochemical characterization results

The electrochemical behaviour of the $NaMnPO_4$-CNF cathode is first evaluated by cyclic voltammetry. The voltammograms recorded between 1.0 and 3.5 V vs. $Na/Na^+$ at 0.1 mV $s^{-1}$ (Fig. 5a) show two pairs of redox peaks, with oxidation at ~2.6 V and ~ 3.1 V and reduction at ~2.7 V and ~ 2.2 V, attributable to the $Mn^{2+}/Mn^{3+}$ Faradaic transitions associated with reversible $Na^+$ (de)intercalation within the $NaMnPO_4$ structure [31]. The presence of two distinct redox pairs suggests the contribution of multiple electrochemical processes within the biphasic $NaMnPO_4$ system. In particular, the higher-potential redox couple (~3.1/2.7 V) can be plausibly associated with the olivine-type phase, which is known to exhibit higher electrochemical activity due to its open framework enabling $Na^+$ intercalation. The relatively sharper and more symmetric shape of this pair is consistent with a bulk intercalation mechanism. In contrast, the lower-potential redox features (~2.6/2.2 V) may be related to the maricite-type phase. Although maricite is generally considered electrochemically inactive in bulk form due to the absence of efficient $Na^+$ diffusion pathways, its nanoscale dispersion within the conductive CNF matrix and its interaction with the olivine phase may facilitate $Na^+$ transport, enabling a detectable Faradaic response. The broader shape of this pair is consistent with a more sluggish and/or surface-assisted process. While a fully unambiguous assignment of each redox pair to a specific phase remains complex, the observed electrochemical features are consistent with the biphasic composition identified by XRD and Rietveld refinement, supporting the proposed interpretation. The broadness of the peaks, combined with the quasi-rectangular shape of the voltammogram, further suggests the coexistence of pseudocapacitive effects and diffusion-controlled intercalation processes. This behaviour is typical of nanostructured materials with high surface area and porosity, in good agreement with the porous $NaMnPO_4$–CNF architecture described above. The good overlap of the CV curves over five consecutive cycles confirms the structural integrity and reversibility of the redox reactions. To further elucidate the charge storage mechanism, CV measurements were performed at different scan

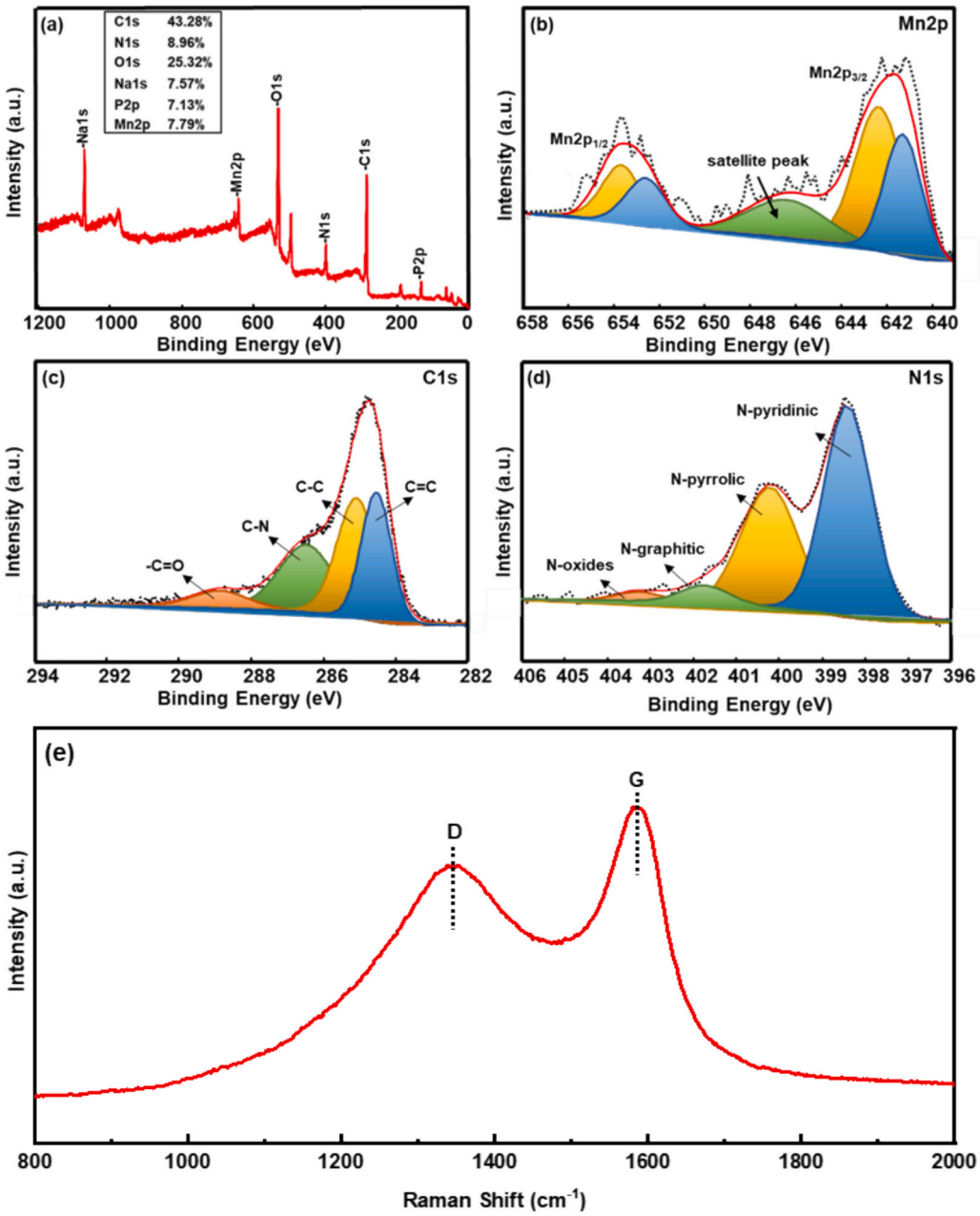


**Fig. 4.** XPS and Raman characterization of the $NaMnPO_4$–CNF electrode: (a) survey spectrum; (b) Mn 2p; (c) C 1 s; (d) N 1 s; (e) Raman spectrum showing the characteristic D and G bands of the carbon nanofiber matrix.

rates ranging from 0.1 to 2.0 mV $s^{-1}$ (Fig. 5b). The selected scan rate range (0.1–2.0 mV $s^{-1}$) is consistent with commonly adopted values for Na-ion battery cathodes and is sufficient to reliably probe the charge storage mechanism. As the scan rate increases, the current response correspondingly rises, accompanied by a slight broadening of the redox peaks and increased polarization, indicating the coexistence of diffusion-controlled and surface-controlled processes. The relationship between peak current (i) and scan rate (v) follows the power-law equation $i = a\ v^b$, where the b-value provides insight into the dominant charge storage mechanism. As shown in Fig. 5c, the calculated b-values range from 0.68 to 0.99, indicating a mixed contribution from diffusion-controlled intercalation and surface-controlled (pseudocapacitive) behaviour. Notably, the b-value close to unity (~0.99) suggests a quasi-pseudocapacitive response for the corresponding redox process, indicative of fast surface-controlled kinetics facilitated by the conductive CNF network. To quantitatively distinguish these contributions, Dunn's method is applied (Fig. 5d). The capacitive contribution increases from ~18% at 0.1 mV $s^{-1}$ to ~50% at 2.0 mV $s^{-1}$, confirming that surface-controlled processes become progressively dominant at higher scan rates. These values fall within the range commonly reported for hybrid battery-type electrode materials, where both diffusion-controlled and pseudocapacitive processes coexist. This behaviour can be attributed to the high specific surface area and the presence of an interconnected N-doped carbon nanofiber network, which promote rapid charge transfer and enhance the electrochemical kinetics of the composite electrode.

Galvanostatic charge–discharge measurements further clarify the electrochemical performance at different current rates. The rate performance is evaluated at increasing current densities of 0.1C, 0.5C, 1C, and 2C, as illustrated in the charge–discharge profiles (Fig. 6a-d) over five consecutive cycles. At 0.1C (Fig. 6a), the material delivered a high initial charge capacity of about 154 mAh $g^{-1}$, which stabilizes around

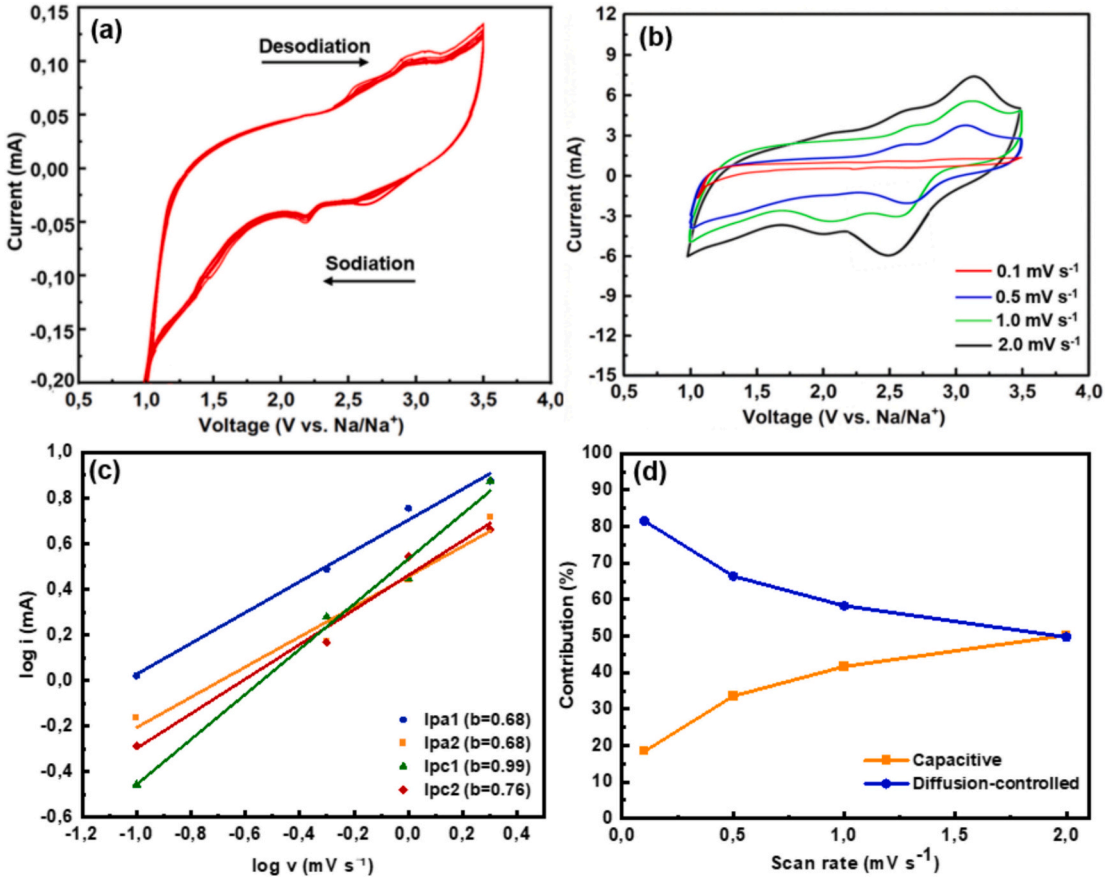


**Fig. 5.** (a) Cyclic voltammetry (CV) curve at 0.1 mV $s^{-1}$ in the potential window of 1.0–3.5 V vs. $Na/Na^+$. (b) CV curves at different scan rates (0.1–2.0 mV $s^{-1}$). (c) log(i) vs log(v) plots with corresponding b-values. (d) Capacitive and diffusion-controlled contributions estimated by Dunn's method.

142 mAh $g^{-1}$ after the fifth cycle. The specific initial discharge capacity reaches ~143 mAh $g^{-1}$, very close to the theoretical capacity (155 mAh $g^{-1}$), and the coulombic efficiency exceeds 95% from the second cycle onward confirming the excellent reversibility and stability of the redox processes. The slight capacity loss in the first cycle is likely due to the formation of a solid electrolyte interface (SEI) and a minor electrolyte decomposition, as commonly observed in Na-ion systems. When the rate increases to 0.5C (Fig. 6b), the voltage profiles retain the same shape observed at 0.1C, demonstrating stable reaction kinetics. The specific discharge capacity decreases to 135 mAh $g^{-1}$ (87% of theoretical), while Coulombic efficiency remains about 96%, confirming efficient transport of ions and electrons even at higher rates. These results reflect the advantages of the electrospun architecture, where the porous CNF network provides continuous conductive pathways, short diffusion lengths and a large electrode–electrolyte interface, while nitrogen doping enhances electronic conductivity and introduces additional $Na^+$ adsorption sites. In addition, the pseudocapacitive contribution identified from CV analysis (Fig. 5c,d) further supports the improved rate capability, as surface-controlled processes facilitate fast charge storage at higher current densities. At higher current densities, the voltage profiles become more sloped due to increased polarization, yet the electrode retains remarkable capacity and stability, delivering ~110 mAh $g^{-1}$ at 1C (Fig. 6c) (~71% of the theoretical value) and ~ 90 mAh $g^{-1}$ at 2C (Fig. 6d) (~58%), with nearly overlapping charge–discharge curves over five cycles, indicative of excellent reversibility and mechanical integrity. The rate-capability plot in Fig. 6e summarizes the specific capacities extracted from the first five charge–discharge cycles at each current density, corresponding to the profiles shown in Fig. 6a–d. As expected, the capacity decreases with increasing current due to kinetic limitations, yet remains stable within each current step, further confirming the robustness of the electrode architecture under different operating conditions. After cycling at higher current densities, the capacity recovers to ~135 mAh $g^{-1}$ when the rate returned to 0.1C, showing that the capacity losses at 0.5C–2C were dominated by kinetic limitations rather than irreversible structural changes. In addition, the error bars reported in Fig. 6e, calculated from three independently assembled coin cells, confirm the excellent reproducibility of the electrochemical measurements. The small magnitude of the error bars further indicates a high level of consistency among the tested cells.

The long-term cycling performance shown in Fig. 7 (a-d) provides a broader perspective on the behaviour previously observed in the rate-capability tests. At a current density of 0.1C (Fig. 7a), the electrode delivers a stable capacity of approximately 138–140 mAh $g^{-1}$ after 500 cycles. When the current density was increased to 0.5C and 1C (Fig. 7b, c), the electrode retained discharge capacities of ~125 and ~ 105 mAh $g^{-1}$, respectively, and still delivered ~80 mAh $g^{-1}$ at 2C (Fig. 7d), demonstrating excellent rate capability and long-term cycling stability. In all cases, the coulombic efficiency remained above 96%, confirming the high reversibility of the $Mn^{2+}/Mn^{3+}$ redox process and the absence of significant parasitic reactions. The gradual nature of the capacity fading, without quick drops, corroborates the results obtained in short-cycle GCD tests (Fig. 6e) indicating that the specific capacity decay is primarily governed by transport and polarization limitations rather than structural degradation.

The good long-term performance suggests that the $NaMnPO_4$–CNF electrode maintains structural integrity during prolonged cycling. In particular, the gradual capacity fading, together with the full recovery of capacity when the current density is returned to 0.1C, indicates that no major degradation or loss of active material occurs during operation. Such electrochemical behaviour is closely connected to the intrinsic

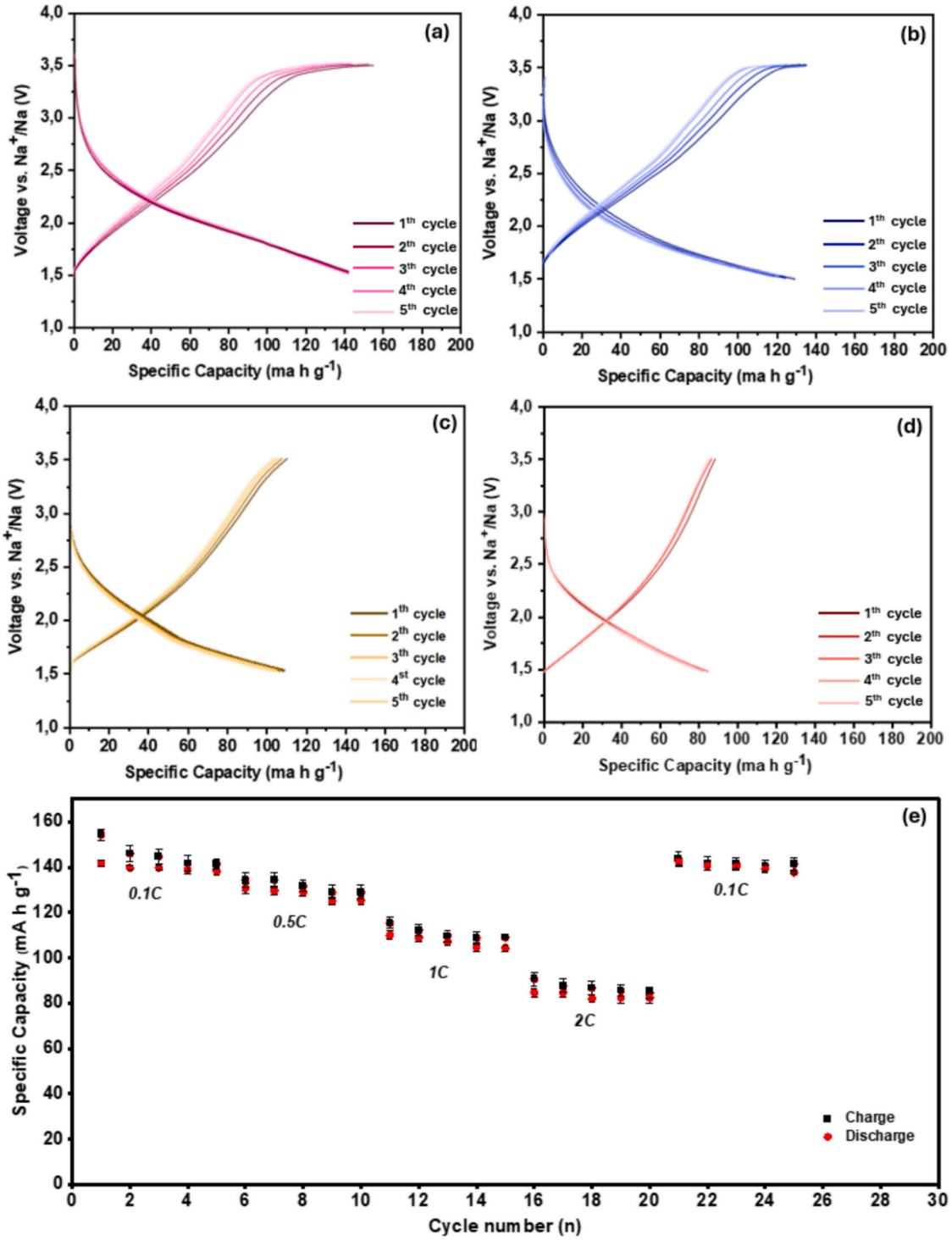


**Fig. 6.** Galvanostatic charge–discharge profiles of the $NaMnPO_4$–CNF electrode at different current densities: (a) 0.1C, (b) 0.5C, (c) 1C, and (d) 2C. (e) Rate capability plot showing the specific capacities at different current densities. Error bars represent the standard deviation from three independently assembled cells.

properties of the electrode architecture. In particular, the electrochemical response can be rationalized considering the synergistic role of the two coexisting $NaMnPO_4$ polymorphs. The olivine-type phase, which represents the dominant fraction (78.7 wt%), is responsible for the reversible $Na^+$ insertion/extraction through the $Mn^{2+}/Mn^{3+}$ redox couple and thus governs the specific capacity. In contrast, the maricite phase (21.3 wt%), although generally considered electrochemically less active due to its unfavourable $Na^+$ diffusion pathways, may contribute to the overall performance by enhancing structural stability and buffering volume changes during cycling. Moreover, the coexistence of the two phases promotes the formation of phase boundaries, which can plausibly facilitate $Na^+$ transport and improve interfacial charge transfer, especially in nanostructured systems. The biphasic architecture may also help to distribute mechanical stress during repeated sodiation/desodiation, thereby contributing to the excellent cycling stability observed. In combination with the conductive CNF network, which ensures efficient electron transport and short diffusion lengths, these effects are expected to contribute to the improved electrochemical

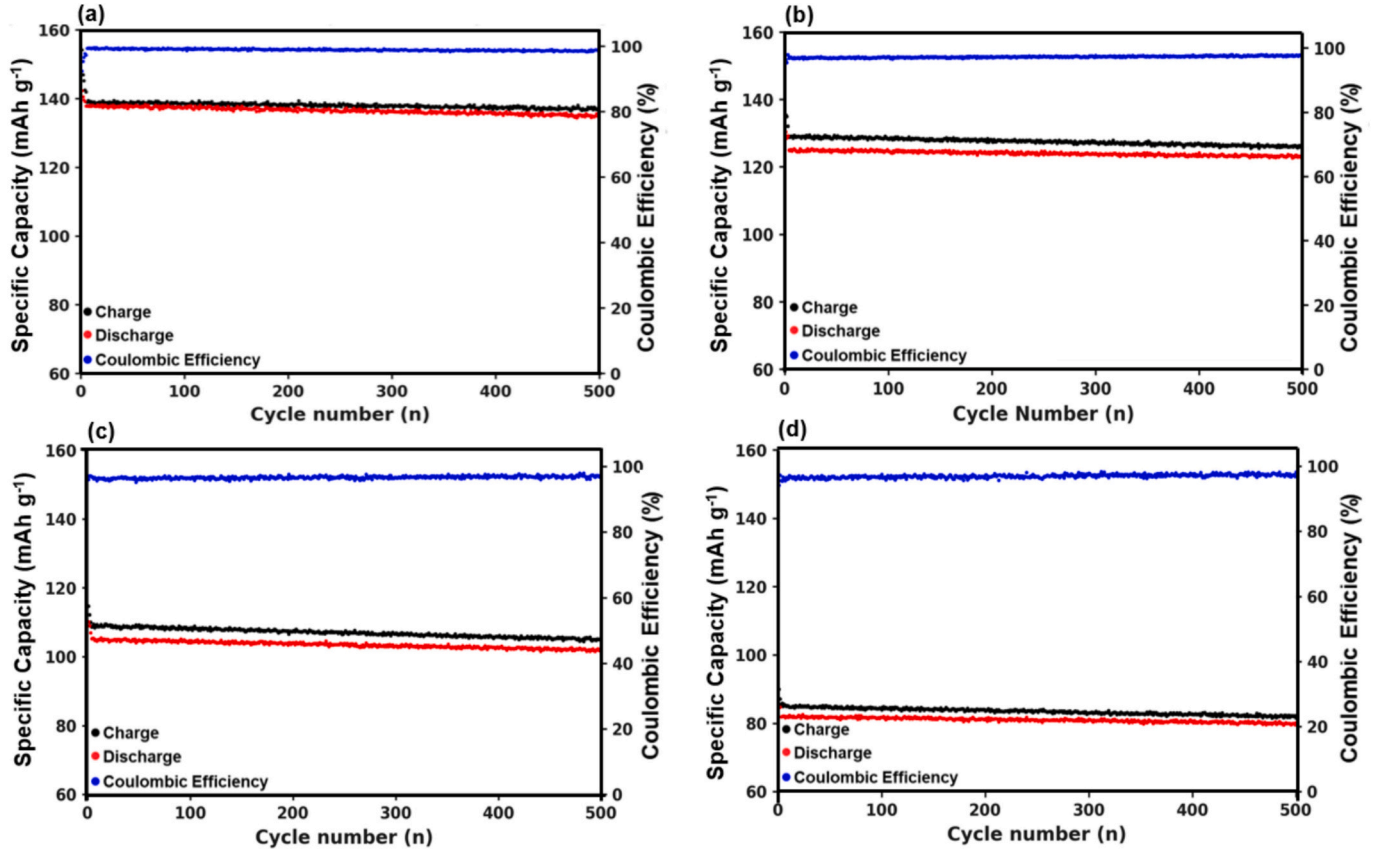


**Fig. 7.** Long-term cycling performance of the $NaMnPO_4$–CNF electrode at different current rates: (a) 0.1C, (b) 0.5C, (c) 1C, and (d) 2C over 500 cycles. The charge/discharge specific capacities and the corresponding coulombic efficiency are shown for each condition.

performance compared to single-phase materials. The coexistence of maricite and olivine phases in the pristine material provides both thermodynamic stability and electrochemical activity, while the CNF network offers continuous electron pathways, reduces mechanical stresses, and prevents particle agglomeration. However, electrochemical cycling can induce progressive structural rearrangements, including partial amorphization, that may influence long-term performance. To clarify how these structural changes relate to the observed stability, a post-mortem comparison between the pristine and cycled electrodes was carried out through XRD, SEM, and EDX analyses. As shown in Fig. 8a, the XRD pattern of the cycled electrode exhibits a broad amorphous diffraction region and a marked attenuation of the crystalline reflections originally associated with the dual maricite–olivine phases. This indicates a gradual loss of long-range order and the formation of an amorphous Na—Mn phosphate phase upon repeated $Na^+$ insertion/extraction. This amorphization does not indicate structural degradation, but rather the formation of a disordered phase capable of accommodating $Na^+$ insertion/extraction, which can help relieve structural strain and contribute to the stable long-term electrochemical performance. SEM images (Fig. 8b-e) reveal that, despite this amorphization, the fibrous CNF architecture remains intact, without fracture or delamination. A direct comparison between pristine and cycled samples at both low and high magnification (Fig. 8b,c vs. Fig. 8d,e) confirms that the overall morphology and surface features are well preserved after prolonged cycling. EDX elemental analysis (Fig. 8f,g) confirmed a homogeneous distribution of Na, Mn, P, and O even after 500 cycles, indicating the absence of phase segregation. The small fluorine contribution is attributed to residual $NaPF_6$. In addition to the signals from the active material and the CNFs, the EDX spectrum in Fig. 8g shows an increased relative intensity of sodium and oxygen, consistent with the presence of residual electrolyte species and SEI components. The apparent variation in the Mn/Na ratio observed after cycling is mainly attributed to surface effects rather than to actual manganese dissolution. In particular, the presence of residual electrolyte species and the formation of a solid electrolyte interphase (SEI) layer lead to an apparent enrichment in Na and O signals, while partially screening the underlying electrode and thus underestimating the Mn contribution in EDX analysis. Since EDX is a surface-sensitive technique, these effects can significantly influence the measured elemental ratios and do not reflect the true bulk composition of the material. The stable electrochemical performance and the absence of significant capacity fading further support that no substantial manganese dissolution occurs during cycling. Overall, the combined structural and electrochemical results indicate that the observed compositional changes are primarily related to interfacial processes and surface reconstruction phenomena, while the bulk active material remains electrochemically stable.

The post-mortem analyses in Fig. 8 confirm the preservation of the electrode morphology after prolonged cycling, despite the progressive amorphization of the $NaMnPO_4$ phase. Therefore, the apparent variation in the Mn/Na ratio is mainly attributed to surface effects rather than to significant manganese dissolution during cycling, as also supported by the stable electrochemical performance. To assess the specific contribution of $NaMnPO_4$, and exclude any significant response from the CNF matrix, the electrochemical behaviour of pristine CNFs was also evaluated, as shown in Fig. 9. The GCD profiles of pristine CNFs (Fig. 9b) were collected in the same voltage window used for the $NaMnPO_4$–CNF electrode. The CV curves (Fig. 9a) display the typical rectangular shape associated with electric double-layer capacitance, while the GCD profiles (Fig. 9b) show sloping curves with no redox plateaus, confirming the absence of Faradaic contributions. As shown in Fig. 9c, the specific discharge capacity of pristine CNFs remains below 8 mAh $g^{-1}$ at 0.1C and stabilizes at very low values with minimal charge–discharge

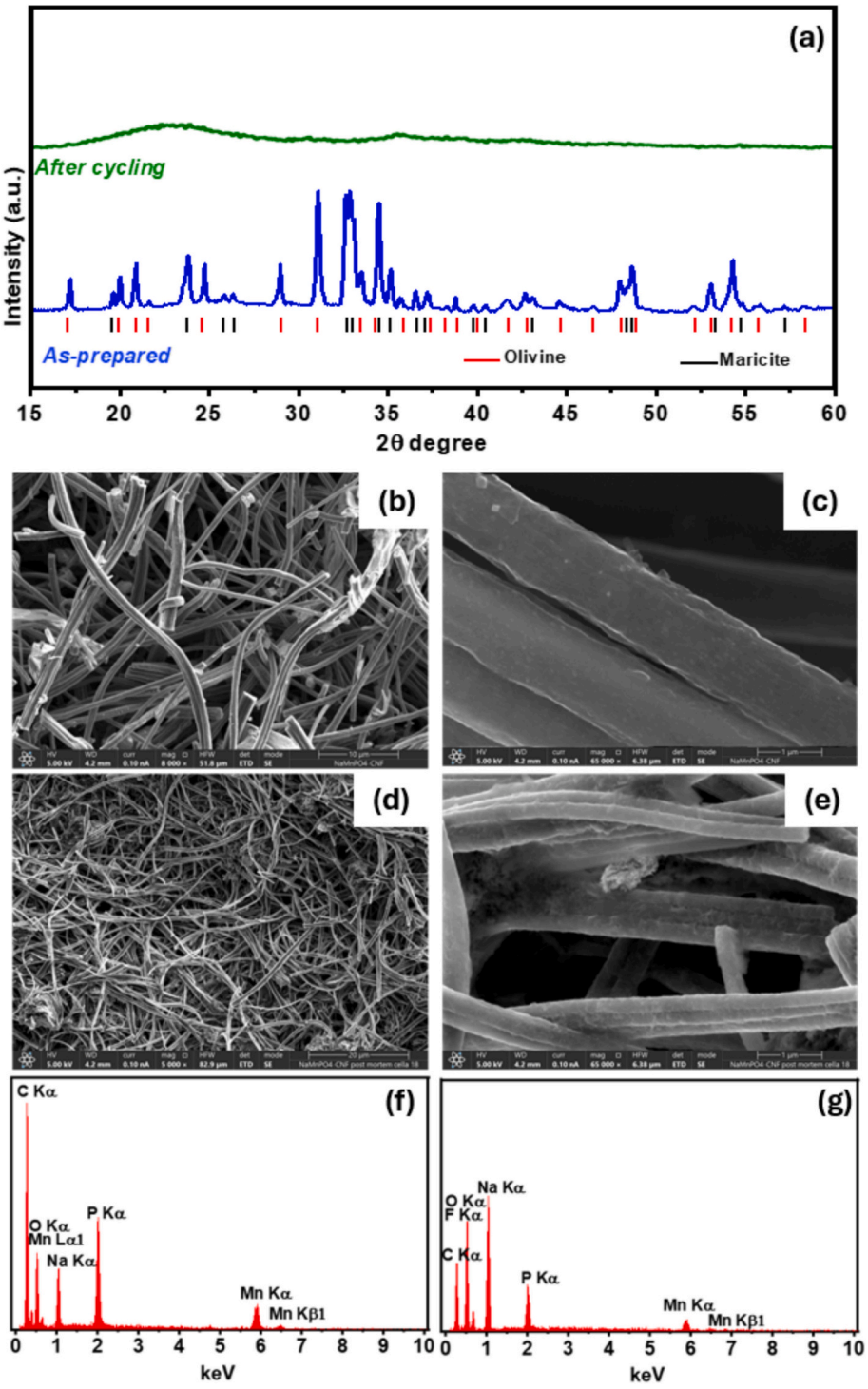


**Fig. 8.** (a) XRD patterns of the as-prepared and cycled sample; (b, c) SEM image of the as-prepared sample at low and high magnification, respectively; (d, e) SEM images of the cycled electrode at low and high magnification, respectively; (f, g) corresponding EDX spectra of the pristine and cycled samples.

hysteresis. These observations clearly indicate that the CNFs do not provide significant Faradaic contribution to the overall capacity. Therefore, the electrochemical performance of the $NaMnPO_4$–CNF composite arises almost entirely from the $NaMnPO_4$ phase, and all specific capacity values reported in this work are calculated with respect to the active $NaMnPO_4$ mass.

To further assess the relevance of the obtained results, Table 2 compares the performance of the $NaMnPO_4$–CNF electrode with Mn-based phosphate cathodes reported in the literature [28–31]. Since most maricite $NaMnPO_4$ electrodes have been evaluated only at low current densities, the comparison is carried out at 0.1C, which represents the highest C-rate reported for these materials. At this C-rate the freestanding $NaMnPO_4$–CNF composite clearly outperforms conventional slurry-cast maricite electrodes, which typically deliver a discharge capacity of 30–102 mAh $g^{-1}$ with limited cycling stability. In contrast, our electrode achieves ~143 mAh $g^{-1}$ at 0.1C, close to the theoretical capacity, and retains excellent stability over 500 cycles. These results, combined with the binder-free and current-collector-free configuration,

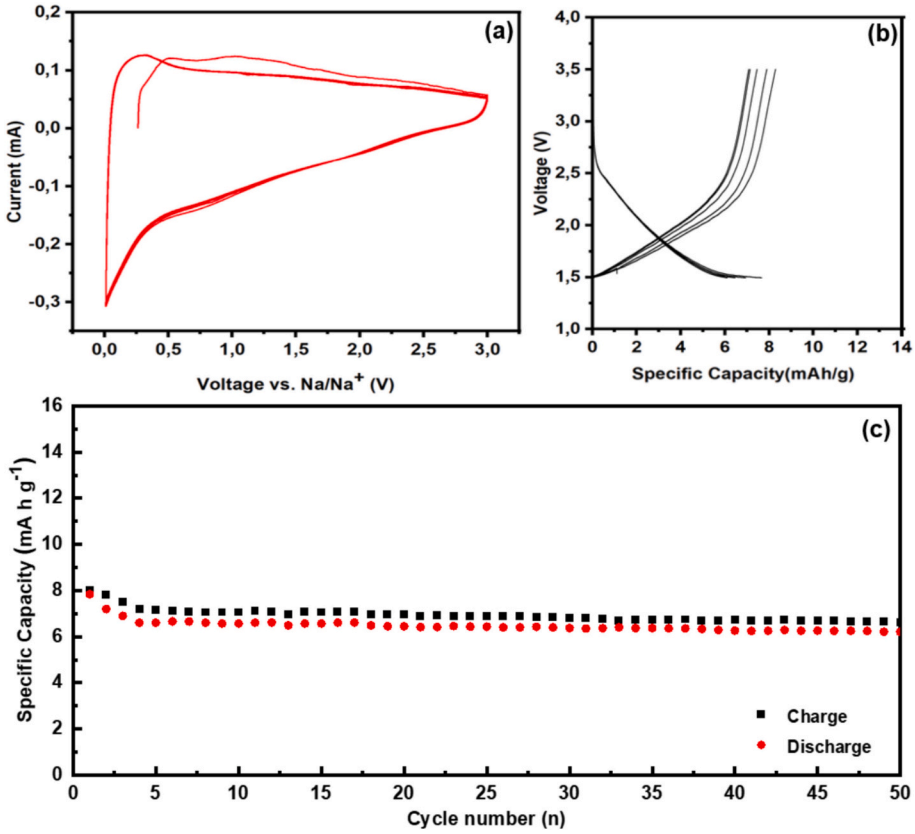


**Fig. 9.** Electrochemical performance of PAN-derived carbon nanofibers (CNFs): (a) CV curves at 0.1 mV $s^{-1}$; (b) GCD profiles in the voltage range of 1.5–3.5 V vs. $Na^+/Na$ at 0.1C; (c) Cycling performance over 50 cycles at 0.1C.

**Table 2**
Comparison between the freestanding $NaMnPO_4$–CNF electrode developed in this work and Mn-based phosphate cathodes reported in the literature.

| Reference | Material / Architecture | Electrode Design | Voltage Window / Electrolyte/ Separator | C-rate | Discharge Specific Capacity (mAh $g^{-1}$) | Cycling / Retention |
|---|---|---|---|---|---|---|
| This work ($NaMnPO_4$–CNF) | $NaMnPO_4$ nanoparticles embedded in N-doped CNFs | Freestanding, binder-free | 1.5–3.5 V; 1 M $NaPF_6$ in EC/DEC GF/A separator | 0.1C | ~143 | 500 cycles: ~138 mAh $g^{-1}$ @0.1C; coulombic efficiency >96% |
| Mohsin et al., Int. J. Electrochem. 2023 [28] | Maricite $NaMnPO_4$ (commercial, ball-milled + carbon coating) | Slurry on Al foil, PVdF + carbon black + active material | 1.0–4.5 V; $NaClO_4$ in EC:DMC + FEC | 0.1C | ~47 | n.d. |
| Priyanka et al., Appl. Nanoscience 2020 [29] | Nanosized maricite $NaMnPO_4$ (solid-state synthesis + ball milling) | Slurry on Al foil, PVdF + carbon black + active material | 0.5–4.0 V; 1 M $NaPF_6$ in PC | 0.1C | ~30 | 50 cycles: ~18 mAh $g^{-1}$ @0.1C; coulombic efficiency~82% |
| Priyanka et al., Ind. Eng. Chem. Res. 2021 [30] | Maricite $NaMnPO_4$ via polyol (different diols/PEG) | Slurry on Al foil, PVdF + carbon black + active material | 1.5–4.5 V; 1 M $NaClO_4$ in PC | 0.1C | ~102 | 50 cycles: ~70 mAh $g^{-1}$ @0.1C; coulombic efficiency~96% |
| Priyanka et al., JSSC 2020 [31] | Maricite $NaMnPO_4$ nanorods (polyol synthesis; different manganese precursors) | Slurry on Al foil, PVdF + carbon black+ active material | 1.5–4.5 V; 1 M $NaClO_4$ in PC | 0.1C | ~102 | 100 cycles: ~55 mAh $g^{-1}$ @0.1C; coulombic efficiency~96% |

highlight the strong potential of the $NaMnPO_4$–CNF cathode material for high-performance sodium-ion batteries.

## 4. Conclusions

In this work, a freestanding $NaMnPO_4$–carbon nanofiber cathode was successfully developed through the electrospinning technique followed by thermal treatment, enabling simultaneous phase formation and electrode fabrication without binders, conductive additives, or metal current collectors. Structural and morphological analyses demonstrated the homogeneous dispersion of maricite and olivine $NaMnPO_4$ phases within a porous, N-doped CNF matrix, resulting in a highly interconnected architecture that promotes fast ion transport and continuous electronic pathways. The $NaMnPO_4$–CNF electrode delivered outstanding electrochemical performance, achieving ~143 mAh $g^{-1}$ at 0.1C, close to the theoretical capacity, and retaining ~135, ~110, and ~ 90 mAh $g^{-1}$ at 0.5C, 1C, and 2C, respectively, with Coulombic efficiencies above 95%. Long-term cycling confirmed remarkable durability, with ~140 mAh $g^{-1}$ at 0.1C, ~125 mAh $g^{-1}$ at 0.5C and ~ 80 mAh $g^{-1}$ at 2C after 500 cycles. Charge-discharge tests on pristine CNFs verified that the measured capacity originates almost entirely from the $NaMnPO_4$ phase. Post-mortem XRD and SEM/EDX analyses revealed

that prolonged cycling leads to a progressive amorphization of the $NaMnPO_4$ phase, while the CNF network preserves the fibrous morphology and elemental homogeneity. This stability arises from the synergistic interaction between the maricite–olivine dual phase and the conductive, mechanically robust CNF matrix, which accommodates volume changes and prevents particle agglomeration. Compared to previously reported maricite $NaMnPO_4$ cathodes, our freestanding $NaMnPO_4$–CNF electrode exhibits superior specific capacity, rate capability, and cycling stability at the same C-rate and even at higher current densities. The combination of high performance, simplified processing, and binder- and current collector-free design makes this electrospun architecture a promising candidate for flexible, energy-dense, and cost-effective sodium-ion batteries.

## CRediT authorship contribution statement

**Leone Frusteri:** Writing – review & editing, Data curation, Conceptualization. **Emanuele La Mazza:** Writing – review & editing, Data curation, Conceptualization. **Mayank Joshi:** Methodology, Investigation, Data curation. **Orazio Di Blasi:** Methodology, Investigation, Data curation. **Alessandra Di Blasi:** Visualization, Project administration, Funding acquisition. **Concetta Busacca:** Writing – review & editing, Writing – original draft, Validation, Supervision, Conceptualization.

## Declaration of Generative AI and AI-assisted technologies in the writing process

During the preparation of this work the authors used ChatGPT (OpenAI) for proofreading and formal language adjustments. After using this tool/service, the authors reviewed and edited the content as needed and take full responsibility for the content of the published article.

## Declaration of competing interest

The authors declare that they have no known competing financial interests or personal relationships that could have appeared to influence the work reported in this paper.

## Acknowledgements

Authors acknowledge the financial support of “la Ricerca di Sistema elettrico Nazionale” by Accordo di Programma (AdP) MASE-CNR PTR 22-24 – “1.2 Progetto Integrato tecnologie di accumulo elettrochimico e termico”.

## Data availability

Data will be made available on request.

## References

[1] A.O.M. Maka, T. Ghalut, E. Elsaye, The pathway towards decarbonisation and net-zero emissions by 2050: the role of solar energy technology, Green Technol. Sustain. 2 (2024) 100107, https://doi.org/10.1016/j.grets.2024.100107.
[2] Q. Hassan, P. Viktor, T.J. Al-Musawi, B. Mahmood Ali, S. Algburi, H.M. Alzoubi, A. Khudhair Al-Jiboory, A. Zuhair Sameen, H.M. Salman, M. Jaszczur, The renewable energy role in the global energy transformations, Renew. Energy Focus 48 (2024) 100545, https://doi.org/10.1016/j.ref.2024.100545.
[3] A.G. Olabi, M.A. Abdelkareem, Energy storage systems towards 2050, Energy 219 (2021) 119634, https://doi.org/10.1016/j.energy.2020.119634.
[4] A.A. Kebede, T. Kalogiannis, J. Van Mierlo, M. Berecibar, A comprehensive review of stationary energy storage devices for large scale renewable energy sources grid integration, Renew. Sustain. Energy Rev. 159 (2022) 112213, https://doi.org/10.1016/j.rser.2022.112213.
[5] P. Saini, L. Gidwani, An investigation for battery energy storage system installation with renewable energy resources in distribution system by considering residential, commercial and industrial load models, J. Energy Storage 45 (2022) 103493, https://doi.org/10.1016/j.est.2021.103493.
[6] S.B. Wali, M.A. Hannan, M.S. Reza, P.J. Ker, R.A. Begum, M.S.A. Rahman, M. Mansor, Battery storage systems integrated renewable energy sources: a biblio metric analysis towards future directions, J. Energy Storage 35 (2021) 102296, https://doi.org/10.1016/j.est.2021.102296.
[7] H.S. Hirsh, Y. Li, D.H.S. Tan, M. Zhang, E. Zhao, Y.S. Meng, Sodium-ion batteries paving the way for grid energy storage, Adv. Energy Mater. 10 (2020) 2001274, https://doi.org/10.1002/aenm.202001274.
[8] L. Zhao, T. Zhang, W. Li, T. Li, L. Zhang, X. Zhang, Z. Wang, Engineering of sodium-ion batteries: opportunities and challenges, Engineering 24 (2023) 172–183, https://doi.org/10.1016/j.eng.2021.08.032.
[9] A.K.X. Tan, S. Paul, Beyond Lithium: future battery technologies for sustainable energy storage, Energies 17 (2024) 5768, https://doi.org/10.3390/en17225768.
[10] A. Nekahi, M. Dorri, M. Rezaei, M.D. Bouguern, A.K. Madikere Raghunatha Reddy, X. Li, S. Deng, K. Zaghib, Comparative issues of metal-ion batteries toward sustainable energy storage: lithium vs. sodium, Batteries 10 (2024) 279, https://doi.org/10.3390/batteries10080279.
[11] J. Chen, G. Adit, L. Li, Y. Zhang, D.H.C. Chua, P.S. Lee, Optimization strategies toward functional sodium-ion batteries, Energy Environ. Mater. 6 (2023) e12633, https://doi.org/10.1002/eem2.12633.
[12] S. Mukherjee, S. Bin Mujib, D. Soares, G. Singh, Electrode materials for high-performance sodium-ion batteries, Materials 12 (2019) 1952, https://doi.org/10.3390/ma12121952.
[13] M. He, S. Liu, J. Wu, J. Zhu, Review of cathode materials for sodium-ion batteries, Prog. Solid State Chem. 74 (2024) 100452, https://doi.org/10.1016/j.progsolidstchem.2024.100452.
[14] Y. Fang, X.-Y. Yu, X.W. (David) Lou, Nanostructured electrode materials for advanced sodium-ion batteries, Matter 1 (2019) 90–114, https://doi.org/10.1016/j.matt.2019.05.007.
[15] X.-H. Liu, W.-H. Lai, S.-L. Chou, The application of hollow micro−/nanostructured cathodes for sodium-ion batteries, Mater. Chem. Front. 4 (2020) 1289–1303, https://doi.org/10.1039/C9QM00674E.
[16] L. Mai, J. Sheng, L. Xu, S. Tan, J. Meng, One-dimensional hetero-nanostructures for rechargeable batteries, Acc. Chem. Res. 51 (2018) 950–959, https://doi.org/10.1021/acs.accounts.8b00031.
[17] A. Machín, K. Fontánez, J.C. Arango, D. Ortiz, J. De León, S. Pinilla, V. Nicolosi, F. I. Petrescu, C. Morant, F. Márquez, One-dimensional (1D) nanostructured materials for energy applications, Materials 14 (2021) 2609, https://doi.org/10.3390/ma14102609.
[18] L. Wang, G. Yang, S. Peng, J. Wang, W. Yan, S. Ramakrishna, One-dimensional nanomaterials toward electrochemical sodium-ion storage applications via electrospinning, Energy Storage Mater. 25 (2020) 443–476, https://doi.org/10.1016/j.ensm.2019.09.036.
[19] Y. Wang, Y. Liu, Y. Liu, Q. Shen, C. Chen, F. Qiu, P. Li, L. Jiao, X. Qu, Recent advances in electrospun electrode materials for sodium-ion batteries, J. Energy Chem. 54 (2021) 225–241, https://doi.org/10.1016/j.jechem.2020.05.065.
[20] W. Li, L. Zeng, Y. Wu, Y. Yu, Nanostructured electrode materials for lithium-ion and sodium-ion batteries via electrospinning, Sci. China-Mater. 59 (2016) 287–321, https://doi.org/10.1007/s40843-016-5039-6.
[21] B. Fu, X. Zhou, Y. Wang, High-rate performance electrospun Na0.44MnO2 nanofibers as cathode material for sodium-ion batteries, J. Power Sources 310 (2016) 102–108, https://doi.org/10.1016/j.jpowsour.2016.01.101.
[22] L. Liang, X. Sun, D.K. Denis, J. Zhang, L. Hou, Y. Liu, C. Yuan, Ultralong layered $NaCrO_2$ nanowires: a competitive wide-temperature-operating cathode for extraordinary high-rate sodium-ion batteries, ACS Appl. Mater. Interfaces 11 (2019) 4037–4046, https://doi.org/10.1021/acsami.8b20149.
[23] W. Ren, M. Qin, Y. Zhou, H. Zhou, J. Zhu, J. Pan, J. Zhou, X. Cao, S. Liang, Electrospun Na4Fe3(PO4)2(P2O7) nanofibers as free-standing cathodes for ultralong-life and high-rate sodium-ion batteries, Energy Storage Mater. 54 (2023) 776–783, https://doi.org/10.1016/j.ensm.2022.11.018.
[24] Y. Liu, N. Zhang, F. Wang, X. Liu, L. Jiao, L. Fan, Approaching the downsizing limit of Maricite $NaFePO_4$ toward high-performance cathode for sodium-ion batteries, Adv. Funct. Mater. 28 (2018) 1801917, https://doi.org/10.1002/adfm.201801917.
[25] 25 WEF_Top_10_Emerging_Technologies_of_2023, (n.d.).
[26] J. Wang, Z. Wang, J. Ni, L. Li, Electrospinning for flexible sodium-ion batteries, Energy Storage Mater. 45 (2022) 704–719, https://doi.org/10.1016/j.ensm.2021.12.022.
[27] S. Li, R. Dong, Y. Li, X. Lu, J. Qian, F. Wu, C. Wu, Y. Bai, Advances in free-standing electrodes for sodium ion batteries, Mater. Today 72 (2024) 207–234, https://doi.org/10.1016/j.mattod.2023.11.013.
[28] I.U. Mohsin, L. Schneider, Z. Yu, W. Cai, C. Ziebert, Enabling the electrochemical performance of maricite-NaMnPO4 and maricite-NaFePO4 cathode materials in

sodium-ion batteries, Int. J. Electrochem. 2023 (2023) 1–9, https://doi.org/10.1155/2023/6054452.
[29] V. Priyanka, G. Savithiri, R. Subadevi, M. Sivakumar, An emerging electrochemically active maricite NaMnPO4 as cathode material at elevated temperature for sodium-ion batteries, Appl. Nanosci. 10 (2020) 3945–3951, https://doi.org/10.1007/s13204-020-01506-8.
[30] P. Venkatachalam, S. Ganesan, S. Rengapillai, S. Marimuthu, Gradual development of maricite $NaMnPO_4$ with the influence of diol chain length on the polyol process of surpassed sodium intercalation, Ind. Eng. Chem. Res. 60 (2021) 5861–5868, https://doi.org/10.1021/acs.iecr.1c00102.
[31] V. Priyanka, G. Savithiri, P. Rajkumar, T. Meenatchi, R. Subadevi, M. Sivakumar, Tweaking the electrochemical activity of maricite NaMnPO4 in sodium batteries using different manganese precursors via polyol method, J. Solid State Chem. 290 (2020) 121551, https://doi.org/10.1016/j.jssc.2020.121551.
[32] V. Koleva, T. Boyadzhieva, E. Zhecheva, D. Nihtianova, S. Simova, G. Tyuliev, R. Stoyanova, Precursor-based methods for low-temperature synthesis of defectless NaMnPO4 with an olivine- and maricite-type structure, CrystEngComm 15 (2013) 9080, https://doi.org/10.1039/c3ce41545g.